2024年度　11）SCOSTEP Visiting Scholar (SVS) Program (in ISEE)　目次詳細

2024　11）SCOSTEP Visiting Scholar (SVS) Program in ISEE
List

6 件

＊所属・職名は2025年3月現在

＊Affiliation and Department displayed are current as of March 2025.

研究代表者 Principal Investigator	所属機関* Affiliation	所属部局* Department	職名* Job title	研究課題名 Project Title	頁 Page	備考 Remarks
Dipjyoti Patgiri	Indian Institute of Technology Roorkee, Uttarakhand, India		graduate-course student	To Investigate the Role of Storm/Substorm time Penetrated Electric Fields on Triggering Mechanism of Nighttime Electrified MSTIDs	329	
Ayushi Nema	Sardar Vallabhbhai National Institute of Technology Surat, Gujarat, India		graduate-course student	Characteristic behavior of SAR arc, STEVE and Red-Green arc during HILDCAA events	331	
Moheb Yacoub Saad	Egypt-Japan University of Science and Technology (E-JUST), Egypt		graduate-course student	Automatic detection of equatorial plasma bubbles in airglow images using two-dimensional principal component analysis and explainable artificial intelligence	334	
Huiting Feng	Tongji University - Shanghai, China and GFZ, Potsdam Germany		graduate-course student	Research on Magnetospheric Processes Corresponding to Special Dayside Auroral Structures	336	
Karla Franchesca Lopez Araujo	Center for Radioastronomy and Astrophysics, Mackenzie Presbyterian University, Brazil		graduate-course student	Pre-flare Conditions of Active Regions and Dynamics of the Solar Flares	338	
Luiz Fillip Rodrigues Vital	National Institute for Space Research, Brazil	DICEP	graduate-course student	INVESTIGATION OF POST-MIDNIGHT EQUATORIAL PLASMA BUBBLES: OBSERVATION AND SIMULATION	340	

To Investigate the Role of Storm/Substorm time Penetrated Electric Fields on Triggering Mechanism of Nighttime Electrified MSTIDs

Dipjyoti Patgiri
Research Scholar
Department of Physics, Indian Institute of Technology Roorkee, Uttarakhand, India

Aim & purpose of the visit

The work carried out in ISEE focuses on the investigation of nighttime medium-scale traveling ionospheric disturbance (MSTID) generated during geomagnetic storms over mid-latitudes. Previously, only a few studies reported observations of nighttime MSTIDs during geomagnetic storms over mid and high latitudes (Kelley et al., 2023; Liu et al., 2020; Nishioka et al., 2009; Zhang et al., 2019, 2022). The present work conducted investigations of an atypically aligned (northeast-southwest) MSTID observed on 17 March 2003 during the recovery phase of a moderate geomagnetic storm. The alignment of the observed MSTID was unusual compared to typical nighttime MSTIDs during geomagnetic quiet nights and has not been observed in the previously reported studies. Effects of substorm-induced electric fields on the MSTID perturbations were also investigated.

Datasets and methods

Primarily, detrended total electron content (DTEC) maps have been used to study spatiotemporal evolution of TEC perturbations caused by MSTID on 17 March 2003. TEC data are obtained from over 1000 dual-frequency (1.57542 and 1.22760 GHz) GPS receivers in Japan operated by the Geospatial Information Authority of Japan. Different ionospheric parameters were obtained from ionosonde stations, Wakkanai (45.39°N, 141.69°E), Kokubunji (35.71°N, 139.49°E), Yamagawa (31.20°N, 130.62°E), and Okinawa (26.68°N, 128.16°E) which are located in Japanese sector. Data from a geomagnetic conjugate ionosonde station, Townsville (19.3°S, 146.7°E), Australia were also utilized in this study. Additionally, cross-track wind data of CHAMP and vertical ion drift measurements by ROCSAT-1 were utilized to examine the background thermospheric wind and vertical ion drifts, respectively.

Results

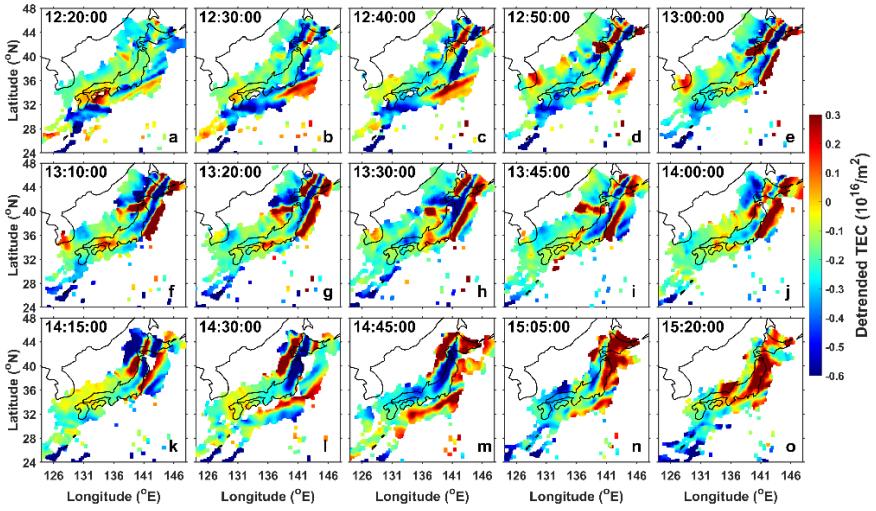

Figure 1: (a-o) DTEC maps over Japan on 17 March 2003.

Figures 1a-o represent the DTEC maps on 17 March. TEC perturbations caused by MSTID with the northeast-southwest alignment of the wavefronts were evident from Figures 1b-n. MSTID was observed during the recovery phase of the storm.

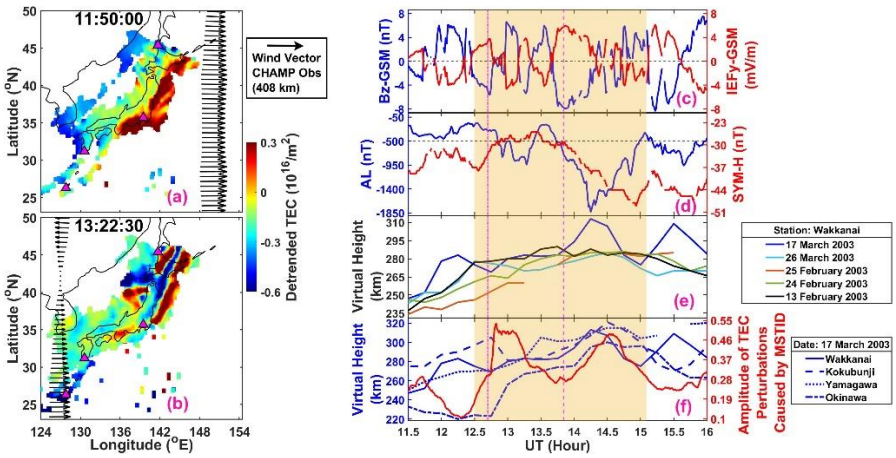

Figure 2: (a-b) Arrows over DTEC maps represent wind direction measured by CHAMP. Temporal variations of (c) IMF-Bz (blue) and IEFy (red), (d) AL (blue) and SYM-H (red), (e) h'F from Wakkanai on 17 March (blue), 23, 24, and 25 February (cyan, orange, & green), and 26 March 2003 (black), (f) h'F from Wakkanai (solid), Kokubunji (dashed), Yamagawa (dotted), & Okinawa (dashed-dotted), and MSTID perturbations amplitude (red-solid), respectively. Triangles in (a-b) & vertical lines and shaded area on (c f) represent the locations of four ionosondes & onset times of two substorms and duration of MSTID observation, respectively.

During the expansion and recovery phases of the second substorm, h'F at Wakkanai on 17 March significantly enhanced and decreased, respectively, compared to other quiet nights (Figures 2d-e). Additionally, h'F at four stations and TEC perturbations amplitude caused by MSTID showed enhancement and decrement concurrently during the expansion and recovery phases of the substorm (Figures 2f).

Period of Stay at ISEE, Nagoya University: From 23 December 2024 to 22 March 2025

References

Kelley, I. J., Kunduri, B. S. R., Baker, J. B. H., Ruohoniemi, J. M., & Shepherd, S. G. (2023). Storm time electrified MSTIDs observed over mid-latitude North America. Journal of Geophysical Research: Space Physics, 128(3), e2022JA031115.

https://doi.org/10.1029/2022JA031115 Liu, Y., Li, Z., Fu, L., Wang, J., & Zhang, C. (2020). Studying the ionospheric responses induced by a geomagnetic storm in September 2017 with multiple observations in America. GPS Solutions, 24, 3. https://doi.org/10.1007/s10291-019-0916-1.

Nishioka, M., Saito, A., & Tsugawa, T. (2009). Super-medium-scale traveling ionospheric disturbance observed at midlatitude during the geomagnetic storm on 10 November 2004. Journal of Geophysical Research, 114(A7), A07310. https://doi.org/10.1029/2008JA013581.

Zhang, S.-R., Erickson, P. J., Coster, A. J., Rideout, W., Vierinen, J., Jonah, O. F., & Goncharenko, L. P. (2019). Subauroral and polar traveling ionospheric disturbances during the 7–9 September 2017 storms. Space Weather, 17, 1748–1764. https://doi.org/10.1029/2019SW002325.

Zhang, S.-R., Nishimura, Y., Erickson, P. J., Aa, E., Kil, H., Deng, Y., et al. (2022). Traveling ionospheric disturbances in the vicinity of storm-enhanced density at midlatitudes. Journal of Geophysical Research: Space Physics, 127, e2022JA030429. https://doi.org/10.1029/2022JA030429.

(Form11-1)

Report

Characteristic behavior of SAR arc, STEVE and Red-Green arc during HILDCAA events

Ayushi Nema
Sardar Vallabhbhai National Institute of Technology, Surat, Gujarat, India
Principal Investigator: Dr. Kazuo Shiokawa,
Professor, Director of ISEE
ISEE, Nagoya University, Japan

1. Purpose

To identify the characteristic behavior of SAR (Stable Auroral Red) arcs, STEVE (Strong Thermal Emission Velocity Enhancements) and Red-Green arcs during HILDCAA (High-Intensity Long-Duration Continuous AE Activity) events during the recovery phase of a geomagnetic storm, using all-sky imagers located at Athabasca (magnetic latitude: 61.1 °N; magnetic longitude: 307.8°W) Canada, Kapuskasing (magnetic latitude: 58.7°N; magnetic longitude: 347.6°W), Canada and Nyrölä (magnetic latitude: 59.4°N; magnetic longitude: 114.9°E), Finland.

2. Methods

HILDCAA events are periods of sustained geomagnetic activity caused by high-speed solar wind streams (HSSs) originating from coronal holes on the Sun. These events are identified by their intensity and extended duration, making them significant for understanding space weather effects on Earth. There are possibilities that HILDCAA events maybe closely linked to various optical and thermal phenomena in the Earth's upper atmosphere, such as SAR arcs, STEVE and Red-Green auroral arcs. We used auroral images from [1] all-sky camera no. 7 in Athabasca, Canada, which was installed on September 3, 2005, [2] all-sky camera no. 16 in Kapuskasing, Canada, which was installed on February 25, 2017, and [3] all-sky camera no. 18 in Nyrölä, Finland, which was installed on January 24, 2017. To identify HILDCAA events, we followed the procedure defined by Tsurutani and Gonzalez in 1987.

S. No.	HILDCAA Start	Start Time (UT)	HILDCAA End	End Time (UT)	Stations
1.	2011/04/30	18:04	2011/05/03	04:56	ATH
2.	2012/05/08	21:22	2012/05/11	06:35	ATH
3.	2015/12/10	00:13	2015/12/12	00:28	ATH
4.	2016/11/24	00:00	2016/11/26	12:03	ATH
5.	2016/12/21	09:41	2016/12/24	18:57	ATH
6.	2017/01/31	08:34	2017/02/04	01:01	ATH
7.	2017/07/24	03:26	2017/07/26	19:06	KAP, ATH
8.	2017/08/17	07:28	2017/08/21	10:24	KAP, ATH, NYR
9.	2018/05/08	14:44	2018/05/11	12:43	ATH, KAP
10.	2019/02/01	02:38	2019/02/03	09:48	KAP, NYR
11.	2019/02/28	05:50	2019/03/02	21:25	KAP, ATH

Table 1. List of HILDCAA events used to observe the occurrence of SAR, STEVE and Red-Green arc

3. Results

Using 630-nm all-sky airglow imagers at Athabasca (Canada), Kapuskasing (Canada) and Nyrölä (Finland), we present the first statistical analysis of the Stable Auroral Red (SAR) arcs, STEVE, and Red-Green (RG) arcs during High-Intensity Long-Duration Continuous AE Activity (HILDCAA) events from 2011 to 2019. These optical phenomena are unique and relatively faint auroral phenomena observed in the Earth's upper atmosphere at subauroral latitudes. We discovered 25 auroral phenomena (SAR arc, STEVE, and Red-Green arc) after analyzing all-sky images taken over a 9-years period from 2011 to 2019. The arc detachments from the auroral oval typically occur in the premidnight sector, indicating ring current ion drift to the dusk sector. We found that more than 90% of HILDCAA events were accompanied by some of these auroras. We also found that these auroras occur predominantly during midnight hours. The occurrence rate of these auroras found to be much higher during HILDCAA events reaching to approximately 45%, compared to previous statistical studies, including non-HILDCAA times.

We prepared keograms and movies of all auroras during these HILDCAA events to study their behavior with and without HILDCAA events by estimating occurrence count. The occurrence count in Fig.1 has been estimated by reading data from its start hour to end hour, excluding cloudy hours when there was no visibility. Before estimations, the recorded hours of each aurora in UT were converted to LT. Each hour was then incremented by 1 count if any of the arc detachment occurred in that hour bin. Total occurrence count was then estimated by summing all the counts in each hour bin. The vertical axis displays the aggregate counts of all auroras in a given time bin, while the horizontal axis displays the local time. The steep rise in occurrence counts during the late evening hours reflects a stronger coupling between solar wind energy.

Fig.2 shows occurrence rate in categorized manner to show the local time distribution of the three types of auroras separately. SAR dominates most time slots, especially during 20-03 LT. RG peaks significantly around 22-00 LT. STEVE occurrences are relatively low but peak around 21-01 LT. The numbers above each bar denotes the total number of observation hours for all phenomena combined with clear sky during that time bin.

This study shows that more than 90% of the analyzed HILDCAA events are associated with at least one of these optical features-SAR arcs, Red-Green auroral arcs, or STEVE. This high correlation underscores the critical role that HILDCAA events may play in creating the magnetospheric and ionospheric conditions necessary for the formation of these visually striking and scientifically significant phenomena. Such results not only affirm the dynamism of HILDCAA events but also highlight their importance in shaping the near-Earth space environment.

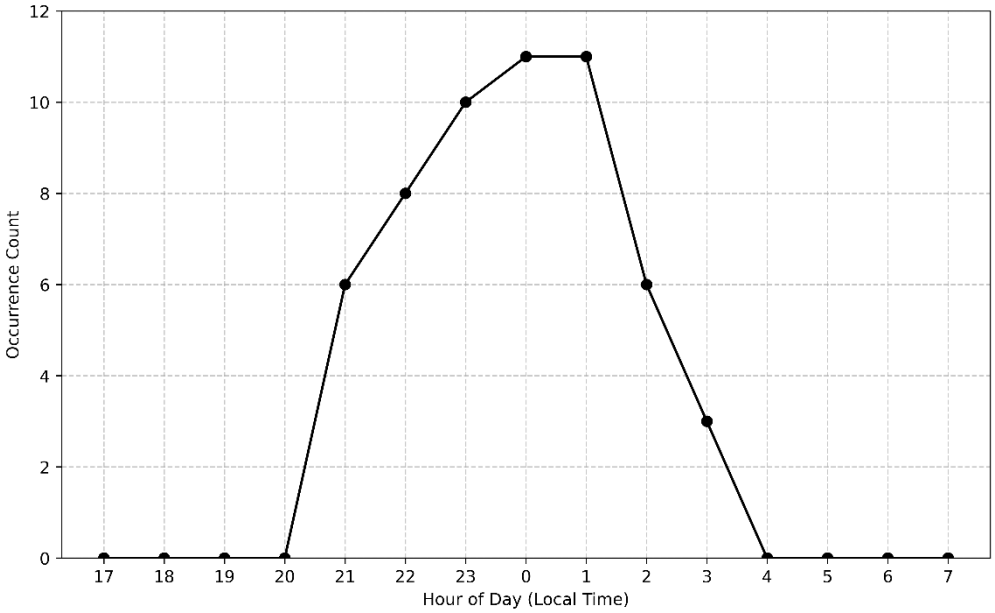

Fig. 1: Occurrence count (in unit of hours) of the observation of SAR, STEVE and Red-Green arcs as a function of local time.

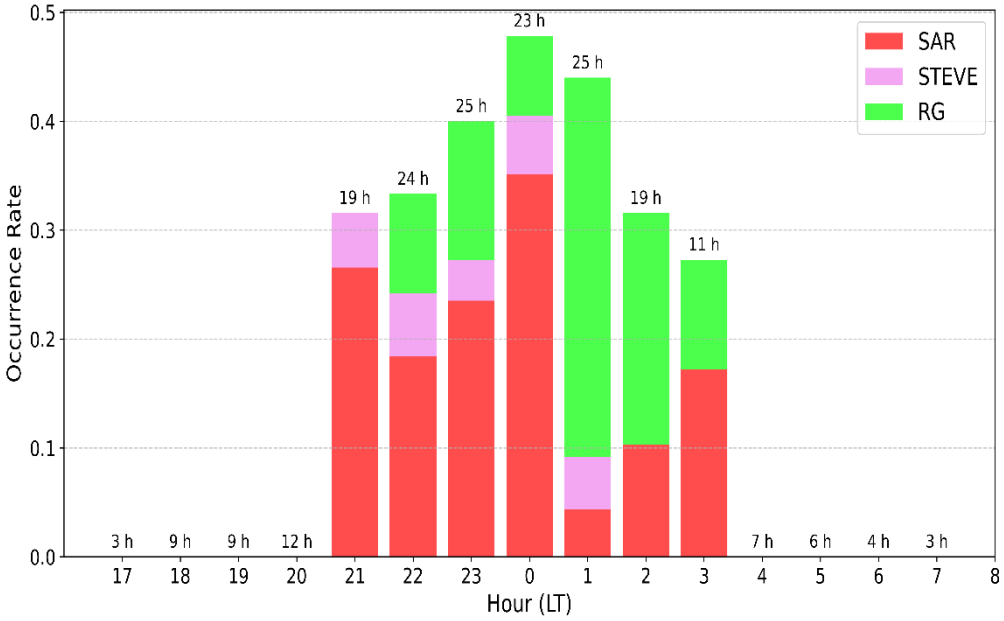

Fig. 2: Occurrence rate variation of SAR, STEVE and Red-Green arcs as a function of local time. Temporal distribution of each auroral event is shown along the bars with red color for SAR arc, purple for STEVE and green for Red-Green arc. The numbers above bars indicate the total hours of available image data with clear sky.

4. Period of stay in ISEE

3 months: 30/09/2024 to 27/12/2024.

5. List of publications

Manuscript under preparation.

(Form11-1)

Automatic detection of equatorial plasma bubbles in airglow images using two-dimensional principal component analysis and explainable artificial intelligence

Moheb Yacoub, Egypt-Japan University of Science and Technology (E-JUST), Researcher

Purpose

During my three-month stay at the Institute for Space-Earth Environmental Research (ISEE), Nagoya University, under the SCOSTEP Visiting Scholar (SVS) Program, I conducted research under supervision of Professor Kazuo Shiokawa on the automatic detection of equatorial plasma bubbles (EPBs) using Explainable Artificial Intelligence (XAI). EPBs are nighttime ionospheric irregularities that significantly affect satellite-based communication and navigation systems. This project aimed to develop a low-computational-cost, accurate, and interpretable model for real-time EPB detection in all-sky imager (ASI) data.

Methods

To achieve these objectives, a novel detection framework was proposed that combines image processing, dimensionality reduction, and machine learning. The main components of the method include:

1. **Dataset Preparation:**

A dataset of 2,458 ASI images were manually classified into two classes “Event” (with EPBs) and “Empty” (without EPBs). The dataset was split into two subsets: 80% for training and 20% for testing.

2. **Dimensionality Reduction:**

Images were transformed using the Radon transform to reduce dimensionality and computational cost.

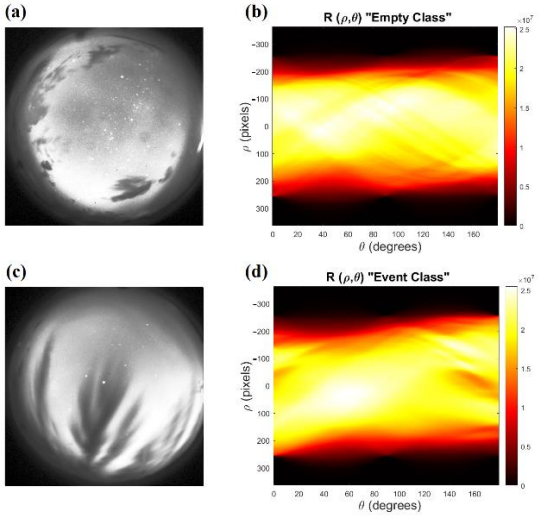

Figure 1. Example of original images and their corresponding Radon-transformed images for samples from each class.

3. **Features Extraction:**

Two-Dimensional Principal Component Analysis (2DPCA) was used to extract significant features from both raw and Radon-transformed images.

4. Model Construction with Explainable AI:

Recursive Feature Elimination (RFE) combined with a Random Forest classifier was applied to rank the most relevant principal components for classification. An ante hoc XAI model was then constructed using only the top contributing components, maximizing performance while minimizing model size.

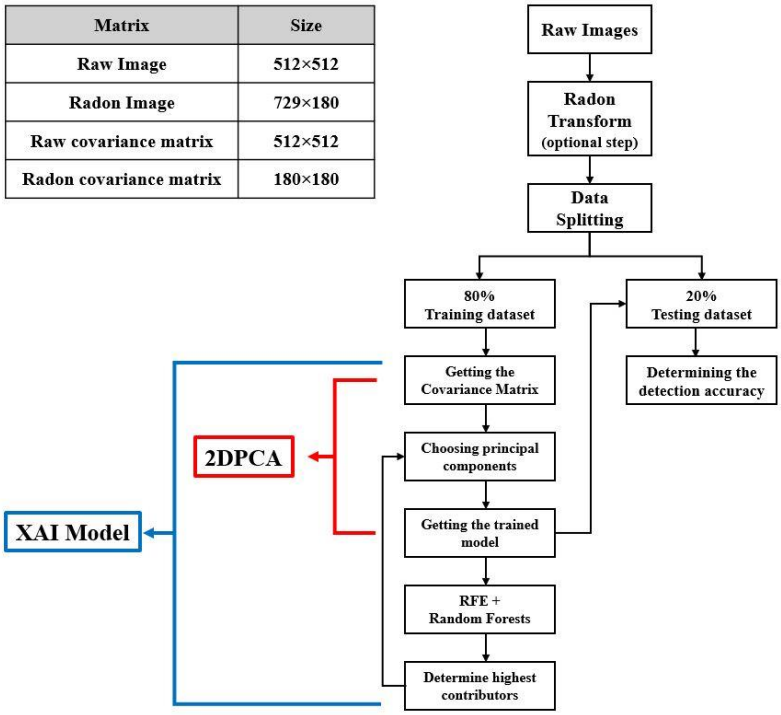

Figure 2. Flowchart of the XAI model with a table of matrix sizes shown in the upper-left corner.

Results

The proposed XAI model achieved excellent performance in detecting equatorial plasma bubbles while maintaining low computational requirements. The model reached a detection accuracy of 98.17% with raw images by combining 2DPCA, RFE, and a Random Forest classifier. A second version, using Radon-transformed images, achieved 97.35% accuracy while reducing the model size and training time by 70%, making it more suitable for real-time and resource-constrained environments. Notably, the explainable design revealed that principal components with smaller eigenvalues could contribute more significantly to classification than expected. The proposed model offered both higher accuracy and significantly faster training compared with another baseline deep learning models, demonstrating its potential for practical deployment in space weather monitoring systems specially in resource-constrained environments.

Publication

Yacoub, M., Abdelwahab, M., Shiokawa, K., & Mahrous, A. (2025). Automatic detection of equatorial plasma bubbles in airglow images using two-dimensional principal component analysis and explainable artificial intelligence. Machine Learning and Knowledge Extraction, 7(1), 26. https://doi.org/10.3390/make7010026.

Research on Magnetospheric Processes Corresponding to Special Dayside Auroral Structures

Principal Investigator Huiting Feng
Affiliation GFZ, Potsdam, Germany
Position Postdoc

Period of Stay in ISEE: 06 April 2025 - 19 April 2025

Research Summary

1. Purpose of the Research

In this study, we aim to conduct a systematic analysis of the possible physical process of afternoon auroral structure by combining data from the Arase satellite, ground-based geomagnetic observations, and auroral and particle precipitation measurements from the Defense Meteorological Satellite Program (DMSP).

2. Methods

To achieve this aim, we first need to select suitable auroral observations from the DMSP/SSUSI data, specifically those in which clear afternoon auroral structures can be identified at the low-latitude boundary of the auroral oval. From these events, we will further select cases where the Arase satellite crosses the afternoon auroral arc. In addition, we will incorporate geomagnetic observations from appropriate ground-based magnetometer stations. By integrating these multi-source observations, we aim to conduct a comprehensive, magnetosphere-to-ionosphere analysis of the afternoon auroral events.

3. Results

In this section, we present the analysis results from one of events identified in our study. As shown in Figure 1(a), this event occurred on November 25, 2017, between 02:00 and 03:00 UT. During this period, DMSP/SSUSI observed an auroral emission enhancement in the low-latitude region of the postnoon auroral oval, and Arase happened to pass through this low-latitude region, as shown in green arrow line. Figures 1(c) - (d) show the precipitating

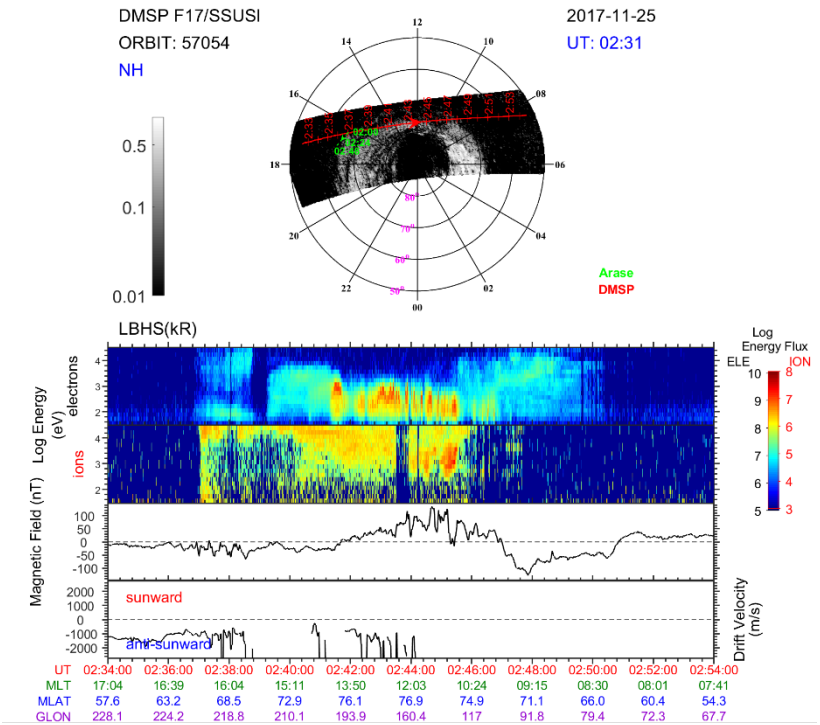

particle distribution and magnetic field variations recorded by DMSP. In this region, we observed precipitating electrons and particles with energies around ~10 keV.

We also plot the magnetic field variations, plasma density, particles and waves distributions from Arase satellite, as shown in Figure 2. From top to bottom, the panels show the magnetic field variations, electron number density, proton, helium, and oxygen electron energy flux distributions, and OFA wave observations.

In addition, we have identified numerous suitable observational events and plan to carry out detailed analyses of selected cases in future work, with the aim of gaining deeper insights into auroral phenomena in the postnoon region.

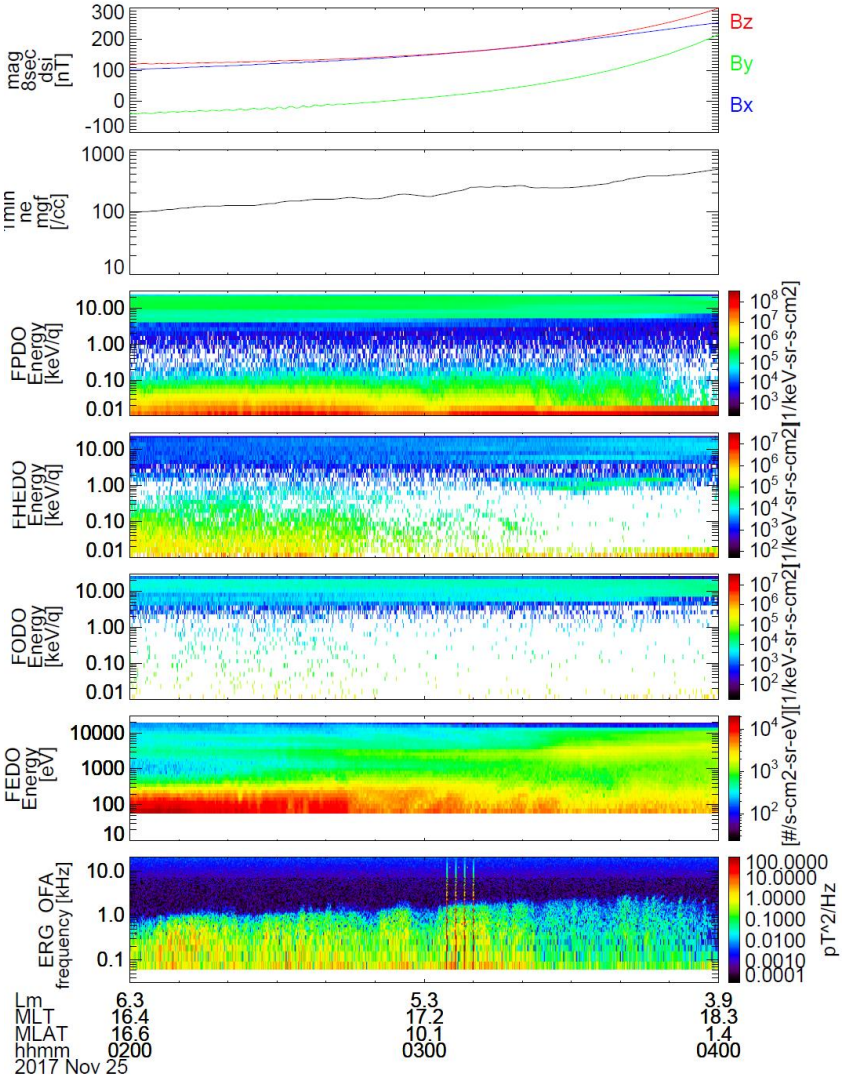

4. Stay at ISEE, Nagoya University

During my visit to Nagoya University, I joined the weekly group meeting of Professor Miyoshi's team and gave a presentation on the conjugate observation event I focused on. I discussed the results with Arase instrument experts and received valuable suggestions, which helped guide the next steps of my research. Based on this collaboration, we plan to write a paper and submit it to a peer-reviewed journal. I also attended academic seminars and exchanged ideas with other group members, which gave me a better understanding of their ongoing research and provided useful perspectives for my own work.

(Form11-1)

Pre-condition of an X1.0 class flare observed on 28 October 2021

Karla Franchesca Lopez Araujo
Mackenzie Presbyterian University, São Paulo - Brazil
Master course ending in December 2024
Supervisors at ISEE: Prof. Kanya Kusano and Prof. KD. Leka

Research Summary:
Solar active regions are areas with high concentrations of magnetic fields, which sometimes can be activated producing solar flares or other eruptive events (e.g., Kazachenko & Hudson 2020). Solar flares consist of sudden explosions that release large amounts of magnetic energy that is converted to other forms, such as bulk motion, plasma heating, and acceleration of particles (Shibata & Magara, 2011; Benz, 2017; Sijie Yu et al., 2020). The dissipation of energy results in the emission of electrons and protons over a wide range of the electromagnetic spectrum extending from radio, infrared, visible, ultraviolet and extreme ultraviolet, X-rays to γ-rays. Solar flares and eruptive events can affect the conditions of the near-Earth environment. Therefore, it is important to understand how active regions evolve and under which conditions produce solar flares.
In this work, I focused on studying an X1.0 class flare that occurred on October 28, 2021 at 15:38:59 UT (peak). The X1.0 class flare was associated with a filament eruption and a coronal mass ejection (CME) as it is shown in Figure 1. During my stay at ISEE, Nagoya University from January 9 to March 25, 2025 guided by Prof. Kusano I studied the pre-flare conditions for the occurrence of the X1.0 class flare. The study was conducted using the **κ**-scheme model (Kusano et al., 2020) applied to the HMI Active Region Patch (SHARP) data remapped to a Lambert Cylindrical Equal-Area projection (SHARP CEA) recorded by SDO/HMI spacecraft (Bobra. et al., 2014). The **κ**-scheme model is based on the nonlinear force-free field (NLFFF) approximation, extrapolated from the vector magnetograms observed by HMI. This model is able to predict large solar flare through considering a "critical condition" of magnetohydrodynamic instability. The critical condition occurs on (or near) the Polarity Inversion Line (PIL) when the magnetic field lines are reconnected producing the double-arc instability (DAI). In other words, the magnetic field becomes unstable with respect to the DAI when a parameter **κ** exceeds a threshold κ_0~0.1. The parameter **κ** is related to the magnetic twist flux density, the area of the reconnection region, and the magnetic flux overlying the double-arc, by which the **κ**-scheme evaluates the critical length scale (r_c) for the region where the trigger-reconnection may happened along the PIL, also it can estimate the magnetic free energy (E_r). This energy means the minimum energy available to be released by the DAI and magnetic reconnection when DAI grows, see more details in Kusano et al., 2020.

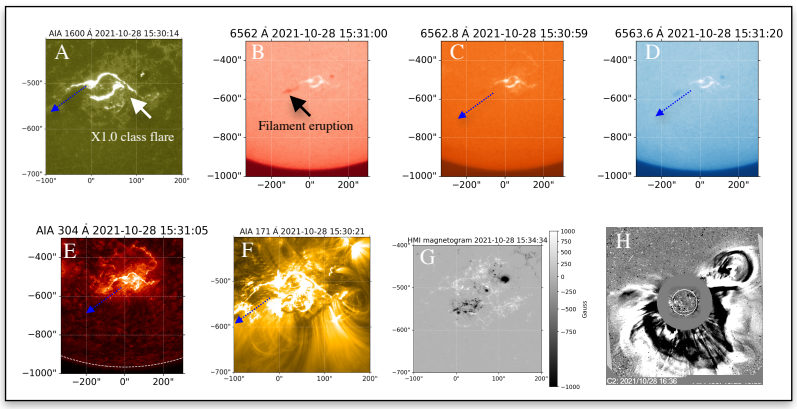

Fig. 1. Multiple wavelengths observation of the active region NOAA-12887 where the X1.0 class flare, filament eruption, and coronal mass ejection (CME) occurred on 28 October 2021. From panel A to F: observations of the solar flare (white arrow) and the filament eruption (black and blue arrow) at 15:30 UT at 1600 Å, Hα -0.8 Å (6562 Å), Hα center (6562.8 Å), Hα +0.8 Å (6563.6 Å), 304 Å, 171 Å taken by the SDO/AIA satellite, the Flare monitoring telescope (FMT), and AIA, respectively.
Panel G: Line of sight (LOS) magnetogram, where the black structures correspond to the negative polarity and the white structures to the positive polarity of the active region NOAA-12887. Panel H: CME observed by LASCO C2 at 16:36 UT.

In this study we address two questions:

1. **Where is the main PIL located?** Figure 2 displays HMI dataset of the active region NOAA-12887 identified as HARP ID 7798 observed on 28 October 2021 at 15:00 UT. From panel A to panel E, we have SHARP data product: Doppler velocity in the Line of Sight (LOS) [m/s], bitmap [dimensionless], disambiguation confidence map [dimensionless], continuum [DN/s], and Line of Sight Magnetogram

$[Mx/cm^2]$, while Panel F displays SHARP CEA data of the radial (out of photosphere) component of the CEA vector magnetic field [SHARP CEA]. Using the data product SHARP and the SHARP CEA data of the radial component (Br), we try to find the main PIL (Figure 2G, white arrow).

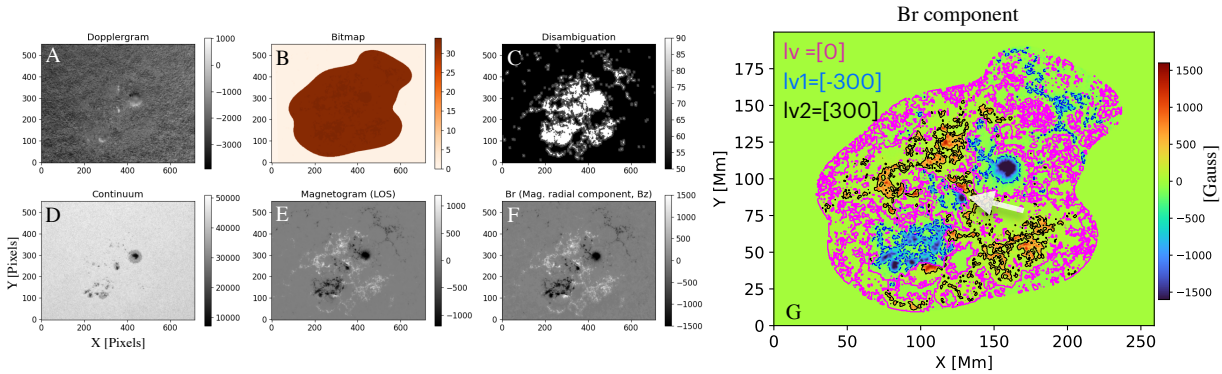

Fig. 2. SHARP and SHARP CEA data product from HARP ID 7798 (NOAA-12887) at 2021.10.28.15_00.00.00 from the hmi_sharp_cea_720s series. Panels from A to E depict the SHARP product: LOS Doppler velocity, bitmap, disambiguation, continuum, and LOS Magnetogram. Panel D: SHARP CEA data of the Br component. Panel G: the "active region pixels" map limited by the bitmap contour level 32 (showing full extent of HMI) of the Br component. The contour maps with level = 0 (magenta) indicate the PIL, which separates the positive and negative polarity, level = -300 (blue) shows the negative magnetic field of 300 Gauss, and level = 300 (black) displays the positive magnetic field of 300 Gauss. The main PIL is point out by the white arrow.

2. **Where does the trigger-reconnection occur during the X1.0 class-flare?** Using the **κ**-scheme model, we found the critical parameters for the region of the trigger-reconnection to become unstable to the DAI along the PIL; the critical length scale r_c and the high free-energy regions HiFERs (E_r), see Figure 3A. In figure 3B is shown the region of the trigger reconnection/HiFER region (pink arrow), which it is located in the main PIL and the high non-potential magnetic field region (1; blue contours) overlaid on the high magnetic twist flux density map on the solar surface. The HiFER region present a twist flux density $T_W \approx 0.75$. Moreover, figure 3C displays the magnetic topology of the active region NOAA-12887 using nonlinear force-free field (NLFFF) extrapolation reproduce in ParaView software, where we observed a quadrupolar active region (light grey tubes) and maybe two filaments/magnetic flux ropes (dark grey and yellow tubes) extended bellow the null-point topology of the quadrupole active region, a similar magnetic characteristics was described by Qiao Song et al., 2023. Furthermore, the magenta contour maps with level = 700 overlaid on the Br component map indicate the high regions of non-potential magnetic field (Bnp), it is also observed in Figure 3B (blue contour maps with same level).

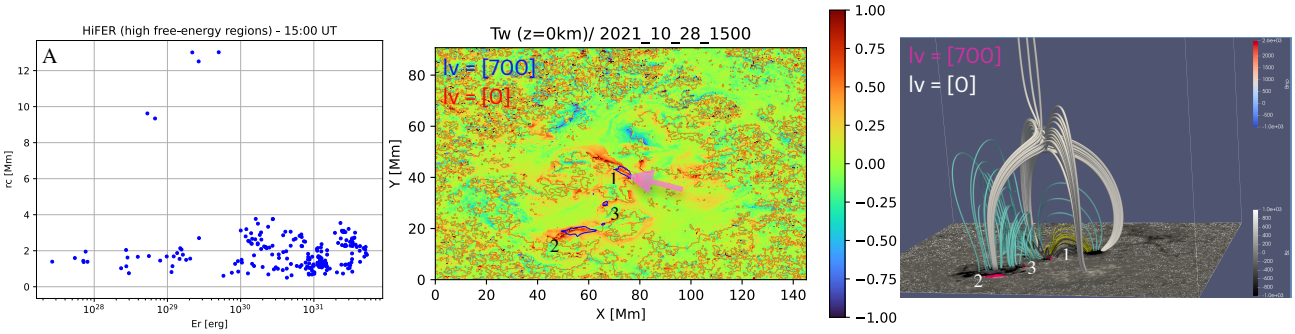

Fig 3. Region of the trigger-reconnection (HiFER region) and the magnetic configuration of the extrapolated coronal magnetic fields of the active region NOAA 12887 at 15:00 UT. Panel A shows the critical parameters r_c and the E_r. Panel B displays the hypothetical HiFER region point out with the pink arrow. Panel C depict the 3D quadrupolar magnetic fields (light grey tubes) above the two filaments or magnetic flux ropes (yellow and dark grey tubes), and the large scale arcades (cyan tubes).

References

Kazachenko M. and Hudson H., 2020. *ApJ* 901 64
Shibata, K. and Magara, T., 2011. *Living Rev. Sol. Phys.* 8, 6
Benz A., 2017. *Living Reviews in Solar Physics,* 5, 1
Yu S., Chen B., Reeves K., Gary D., Musset S., Fleishman G., Nita G., and Glesener L., 2020. *ApJ* 900 17
Bobra M., Sun X., Hoeksema, J., Turmon Y., Liu Y., Hayashi K., Barnes G., and Leka K., 2014. *Sol Phys* 289, 3549–3578
Kusano K., Iju T., Bamba Y., and Inoue S., 2020. *Science* 369, 589-591
Qiao Song, Jing-Song Wang, Xiaoxin Zhang, Hechao Chen, Shuhong Yang, Zhenyong Hou, Yijun Hou, Qian Ye, Peng Zhang, Xiuqing Hu, 2023, ApJ 959 53

(Form11-1)

Report Form of SVS Program

Luiz Fillip Rodrigues Vital, National Institute for Space Research, Brazil

The internship conducted at the Institute for Space-Earth Environmental Research (ISEE) at Nagoya University, under the supervision of Dr. Yuichi Otsuka, was fundamental for the development of my PhD thesis, which examines the probability of occurrence of equatorial plasma bubbles (EPBs). EPBs are large-scale ionospheric irregularities that form in the equatorial and low-latitude regions during the nighttime. In addition to observing EPBs using the rate of total electron content index (ROTI) technique, the Rayleigh-Taylor instability growth rate (γ_{RT})—the main parameter indicating the development of such irregularities—was also calculated.

In this context, the primary objective of my stay at ISEE was to investigate the underlying phenomena driving the occurrence of equatorial plasma bubbles around the local midnight over Brazil. One of the objectives outlined in the initial proposal was to run the GAIA model data to model the γ_{RT} and analyze the results regarding the probability of occurrence. Unfortunately, due to the limited time available to run the analyses, this task was not completed during the internship.

In a second phase, an in-depth analysis was conducted on the effects of post-sunset EPBs, focusing on how the asymmetry of zonal thermospheric winds influences the development of these irregularities. This discussion proved crucial for understanding why the EPB occurrence rate is higher during the September equinox compared to the March equinox. This finding constitutes a new contribution to the literature, as the prevailing theory predicts similar occurrence rates for both equinoxes.

Post-Midnight EPB Event

To investigate the mechanisms associated with the generation of post-midnight EPBs, the night of July 25, 2025, was selected, during which a Medium-Scale Traveling Ionospheric Disturbance (MSTID) likely contributed to the formation of an EPB over northeastern Brazil. Dr. Yuichi Otsuka provided valuable insights into the EPB's development, highlighting its potential interaction with the MSTID, which enhanced the understanding of the mechanisms involved in this specific phenomenon.

The Figure 1 shows a time sequence ofthe 630-nm airglow map observed at (I) São João do Cariri and (II) Bom Jesus da Lapa on the night of July 25, 2022, in Brazil. The original all-sky images were linearized and mapped into geographical coordinates under the assumption that the airglow layer was at an altitude of 250 km. The images cover a horizontal scale of 1536 km, corresponding to a zenith angle of ~75°, with the zenith at the center. The letters 'B' and 'M' markes the plasma bubbles and MSTID, respectively.

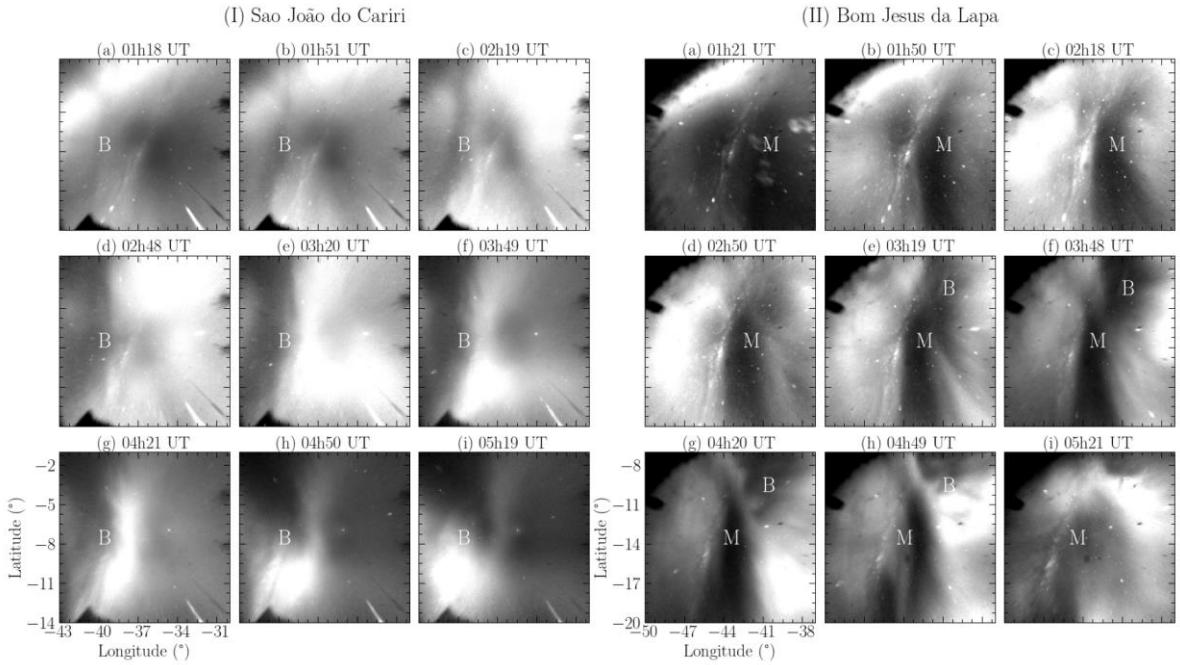

Figure 1 Sequence of unwrapped OI 630,0 nm images obtained at (I) São João do Cariri and (II) Bom Jesus da Lapa show the EPBs ('B' letter) and the MSTID ('M' letter).

This work is still in progress and is expected to be submitted for publication in the coming months. In addition to the analyses of the imager, anomalous signatures in ionospheric parameters obtained from ionosonde data, thermospheric winds through Fabry-Perot interferometer measurements, and satellite data were also investigated.

Seasonal Asymmetry of Post-Sunset EPBs over South America

In this second topic, we benefited from the collaboration of Dr. Balan and Dr. Abadi, whose discussions significantly enriched the scientific results obtained. Both researchers have extensive experience in investigating the seasonal asymmetry of EPBs and thermospheric winds in Southeast Asia, and their substantial contributions were pivotal in interpreting the physical phenomena observed over South America, which form the central focus of my PhD research.

The main result is presented in **Figure 2**, which shows: (a) the occurrence rate of EPBs and (b) the mean γ_{RT} calculated for each season of the year. This analysis considered only geomagnetically quiet periods (Dst > -30 nT), and the June solstice was excluded due to the relatively rare occurrence of EPBs after sunset during this period. The right axis of **Figure 2** (a) and (b) highlights the difference between the September equinox (SE) and the March equinox (ME). The occurrence rate was determined as the ratio of the number of observed EPBs to the total number of days in each season.

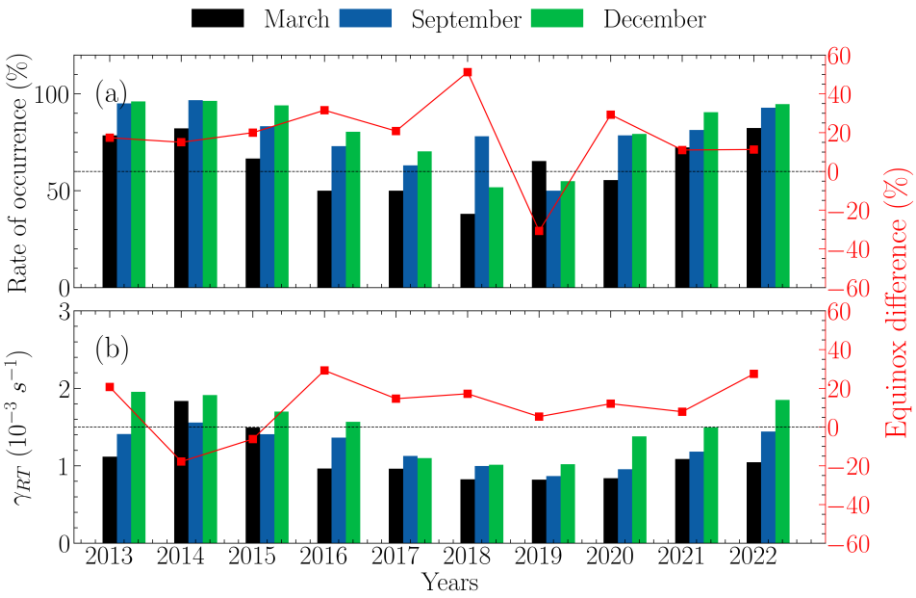

Figure 2 The annual evolution of (a) the post-sunset EPB occurrence rate and (b) the mean γ_{RT} for geomagnetically quiet periods (Dst > -30 nT) in the longitudinal sector of São Luís, Brazil from 2013 to 2022. The black, blue, and green bars represent the Mar.

This latest result was published in my doctoral thesis, which was defended in August 2024. A manuscript based on these findings will soon be prepared and submitted to a journal, with the involvement of all the aforementioned researchers.

Other activities

- During my stay in Japan, I had the opportunity to present the results of my research at COSPAR in Busan, South Korea, in an oral presentation format.
- I conducted seminars for Dr. Otsuka's research group on my research and participated in discussions with other members of the division.
- A significant portion of my time was also dedicated to writing my doctoral thesis, which was in its final stages.
- We made a visit to the MU Radar in Shigaraki.